

ARTICLE OPEN



High-throughput computational-experimental screening protocol for the discovery of bimetallic catalysts

Byung Chul Yeo^{1,2,7}, Hyunji Nam^{3,4,7}, Hyobin Nam^{3,5}, Min-Cheol Kim¹, Hong Woo Lee^{1,4}, Sung-Chul Kim⁶, Sung Ok Won⁶, Donghun Kim¹, Kwan-Young Lee⁴, Seung Yong Lee^{3,5} and Sang Soo Han¹

To accelerate the discovery of materials through computations and experiments, a well-established protocol closely bridging these methods is required. We introduce a high-throughput screening protocol for the discovery of bimetallic catalysts that replace palladium (Pd), where the similarities in the electronic density of states patterns were employed as a screening descriptor. Using first-principles calculations, we screened 4350 bimetallic alloy structures and proposed eight candidates expected to have catalytic performance comparable to that of Pd. Our experiments demonstrate that four bimetallic catalysts indeed exhibit catalytic properties comparable to those of Pd. Moreover, we discover a bimetallic (Ni-Pt) catalyst that has not yet been reported for H₂O₂ direct synthesis. In particular, Ni₆₁Pt₃₉ outperforms the prototypical Pd catalyst for the chemical reaction and exhibits a 9.5-fold enhancement in cost-normalized productivity. This protocol provides an opportunity for the catalyst discovery for the replacement or reduction in the use of the platinum-group metals.

npj Computational Materials (2021)7:137; <https://doi.org/10.1038/s41524-021-00605-6>

INTRODUCTION

One of the important roles of computer simulations in materials science is to predict and/or design materials prior to experiments. In particular, first-principles calculations using density functional theory (DFT) have played a vital role in the field of catalysis^{1–3}. The computational framework enables the prediction or understanding of reaction pathways on catalyst surfaces, which is undoubtedly useful for experimentalists. However, the accurate estimation of some crucial properties such as the reaction barriers on catalytic surfaces is extremely time-consuming in first-principles calculation schemes. In this regard, obtaining a full understanding of the catalytic reaction mechanism via first-principles calculations is often considered rather inefficient. In our experience, although dependent on computing power, a time cost of several months is required for computing a full energetics picture of even one metallic catalyst system. The efficiency of the search of catalysts via first-principles calculations has therefore been questioned because carrying out experimental tests without the aid of computer simulations can often be even faster.

To maximize the efficiency of catalyst discovery using combined computational and experimental studies, the descriptors or features that bridge these two areas should be wisely chosen. Specifically, a simple but physically reasonable descriptor or feature enabling the representation of catalytic properties is critical. A representative example of such a descriptor is the *d*-band center theory that correlates between the *d*-band center⁴, i.e., the average energy of electronic *d*-states projected onto a surface atom of the catalyst, and the gas adsorption energy, which is widely accepted in the field of metallic catalysis. Coupled with the volcano relationship between catalytic activity and adsorption energy⁵, it is theoretically possible to predict catalytic activity from the *d*-band center without exploration of the full reaction

mechanism. Later, along with the *d*-band center theory, consideration of the *d*-band shapes describing higher moments of the *d*-band as well as the *sp*-band properties describing local Pauli electronegativity were also suggested to capture the surface reactivity of transition metal alloys^{6–8}. These studies indicate that the electronic density of states (DOS) patterns themselves projected onto the surface atoms of catalysts can serve as an improved descriptor for the development of metal catalysts because they include more comprehensive information on not only *d*-states but also *sp*-states (both their values and shapes). Nonetheless, the full DOS patterns themselves have never been used as a descriptor in combined computational-experimental screening processes.

As electronic structures are key to determining the physical/chemical properties of materials, materials with similar electronic structures tend to exhibit similar properties. Indeed, a DFT study revealed that a solid-solution Ir₅₀Au₅₀ alloy can exhibit catalytic properties for the H₂ dissociation reaction with an activity comparable to that of Pt, and this result is attributed to the similar electronic structures (DOS patterns) of the Ir₅₀Au₅₀ alloy and Pt⁹. In another example, the similar electronic structures of Rh₅₀Ag₅₀ and Pd were experimentally verified for hydrogen storage¹⁰. The similar electronic structural characteristics enable the Rh₅₀Ag₅₀ alloy to exhibit hydrogen storage properties superior to those of Pd¹¹, although neither Rh nor Ag alone shows hydrogen storage properties⁹. Thus, bimetallic alloys with a DOS pattern similar to that of Pd, which is a well-known representative metal catalyst, should exhibit catalytic performance similar to that of Pd, which is a good hypothesis for the high-throughput development of bimetallic catalysts.

Here, we used the full DOS pattern as a key descriptor in high-throughput computational-experimental screening protocols. As a

¹Computational Science Research Center, Korea Institute of Science and Technology, Seoul, Republic of Korea. ²Department of Energy Resources Engineering, Pukyong National University, Busan, Republic of Korea. ³Materials Architecturing Research Center, Korea Institute of Science and Technology, Seoul, Republic of Korea. ⁴Department of Chemical and Biological Engineering, Korea University, Seoul, Republic of Korea. ⁵Department of Nanomaterials Science and Engineering, Korea University of Science and Technology, Daejeon, Republic of Korea. ⁶Advanced Analysis Center, Korea Institute of Science and Technology, Seoul, Republic of Korea. ⁷These authors contributed equally: Byung Chul Yeo, Hyunji Nam. ✉email: patra@kist.re.kr; sangsoo@kist.re.kr

demonstration in the high-throughput search of bimetallic catalysts, we selected palladium (Pd), the prototypical catalyst for hydrogen peroxide (H_2O_2) synthesis from hydrogen (H_2) and oxygen (O_2) gases^{12–14}, as our reference material. Using DFT calculations, we first screened 4350 crystal structures of bimetallic alloys to investigate their thermodynamic stabilities (only closest-packed surfaces were considered). Next, the similarities in the DOS patterns between the alloys and Pd were quantified, and subsequently, their synthetic feasibility was evaluated. Through these processes, we finally proposed eight candidates with high DOS similarities with Pd, which are expected to show catalytic properties comparable to those of Pd. These eight screened alloys were experimentally synthesized and tested for H_2O_2 direct synthesis, and four of them ($\text{Ni}_{61}\text{Pt}_{39}$, $\text{Au}_{51}\text{Pd}_{49}$, $\text{Pt}_{52}\text{Pd}_{48}$, and $\text{Pd}_{52}\text{Ni}_{48}$) indeed exhibited catalytic properties comparable to those of Pd. In particular, Pd-free $\text{Ni}_{61}\text{Pt}_{39}$ is greatly outperformed prototypic Pd with a 9.5-fold enhancement in cost-normalized productivity (CNP) owing to the high content of inexpensive Ni.

RESULTS

High-throughput computational screening for bimetallic catalysts

Figure 1 shows a schematic diagram of our high-throughput screening protocol for the discovery of bimetallic catalysts. Based on 30 transition metals in periods IV, V, and VI, we considered a total of 435 (${}_{30}\text{C}_2$) binary systems with a 1:1 (50:50) composition. For each alloy combination, 10 ordered phases that are available for 1:1 composition were investigated, namely, B1, B2, B3, B4, B11, B19, B27, B33, L1₀, and L1₁, leading to a screening of 4350 (435×10) crystal structures. Using DFT calculations, we calculated the formation energy (ΔE_f) of each phase and determined which crystal structure is most stable in the bulk phase. Here, negative formation energy implies that the phase is thermodynamically favorable (or that the element combination is miscible), and vice versa. Because nonequilibrium alloyed phases can be stabilized by the nanosize effect, although the elemental combinations are immiscible in the bulk phases^{11,15,16}, a margin of $\Delta E_f < 0.1$ eV was considered when screening the thermodynamic stabilities of the bimetallic systems. The alloyed structures with $\Delta E_f > 0.1$ eV could be readily synthesized; however, such structures would be easily transformed into phase-separated structures during chemical reactions (two-phase structures of the pure elements), which is not suitable for their practical uses as catalysts. Eventually, a total of 435 binary systems and 249 alloys were filtered at the thermodynamic screening step.

For the 249 thermodynamically screened alloys, we calculated the DOS pattern projected on the close-packed surface for each structure and compared it with that of the Pd(111) surface. To quantitatively compare the similarity of two DOS patterns, we defined the following measure:

$$\Delta\text{DOS}_{2-1} = \left\{ \int [\text{DOS}_2(E) - \text{DOS}_1(E)]^2 g(E; \sigma) dE \right\}^{\frac{1}{2}} \quad (1)$$

$$g(E; \sigma) = \frac{1}{\sigma\sqrt{2\pi}} e^{-\frac{(E-E_f)^2}{2\sigma^2}} \quad (2)$$

Here, ΔDOS_{2-1} in Eq. (1) indicates the similarity between the DOS of the alloy (DOS_2) and the DOS of the reference Pd(111) (DOS_1) in which a Gaussian distribution function, $g(E; \sigma)$ in Eq. (2) is considered to compare the two DOS patterns near Fermi energy (E_f) with the high weight. We set the standard deviation, $\sigma = 7$ eV because most of the d -band centers for the bimetallic alloys are distributed from -3.5 eV to 0 eV relative to the Fermi energy.

In comparing two DOS patterns, both d -states and sp -states were considered. To clarify the importance of the inclusion of sp -states, we discuss this effect with an example of O_2 adsorption on

$\text{Ni}_{50}\text{Pt}_{50}(111)$, which is one of the elementary steps for H_2O_2 direct synthesis. In Fig. 2, the DOS patterns for d -states and sp -states are shown; the patterns are obtained by the sum of the partial DOSs of the surface Ni and Pt atoms on $\text{Ni}_{50}\text{Pt}_{50}(111)$. Comparing the DOS patterns before/after O_2 adsorption, the change in the d -band DOS is negligible after O_2 adsorption. On the other hand, the sp -band DOS patterns change more smoothly after O_2 adsorption. This result implies that an O_2 molecule interacts more with the sp -bands of the surface Ni and Pt atoms than with the d -bands on $\text{Ni}_{50}\text{Pt}_{50}(111)$ in O_2 adsorption. The partial DOSs of O_2 before/after O_2 adsorption on $\text{Ni}_{50}\text{Pt}_{50}(111)$ are also compared in Fig. 2. An O_2 molecule in the gas phase has a pair of half-occupied orbitals (π_p^*) in a triplet state, which leads to magnetic properties, resulting from the spin-splitting into up and down states. After O_2 adsorption, the orbitals of the O_2 molecule broaden and the spin-splitting character disappears. Thus, the magnetic moment of the adsorbed O_2 becomes zero (peroxo state), which is supportive evidence that the π_p^* states are fully occupied through the interaction between the metal surface atoms and the O_2 molecule. Then, orbital hybridization between the sp -states of the $\text{Ni}_{50}\text{Pt}_{50}$ surface and the p -states of the O_2 molecule mainly occurs, therefore, consideration of the DOS patterns including the sp -state is required, at a minimum, for H_2O_2 direct synthesis.

The DOS similarity values of the 249 alloy surfaces are shown in Fig. 3. According to the definition of the DOS similarity, as the value approaches zero, the electronic structure of the alloy becomes more similar to that of Pd(111), and the material is expected to show catalytic properties similar to those of Pd(111). In Fig. 3, we chose 17 candidates with the low DOS similarity values ($\Delta\text{DOS}_{2-1} < 2.0$): CrRh ($\Delta\text{DOS}_{2-1} = 1.97$, B2 structure), FeCo (1.63, B2), CoNi (1.71, L1₀), CoHf (1.89, L1₀), CoTa (1.96, L1₀), CoPt (1.78, L1₀), NiCu (1.11, L1₀), NiNb (1.96, L1₀), NiMo (1.87, L1₀), NiRh (0.98, L1₀), Ni-Pd (0.84, L1₀), NiIr (1.28, L1₀), Ni-Pt (1.16, L1₀), CuPd (1.51, B2), RhPt (1.67, L1₀), Pd-Pt (1.16, L1₀), and PdAu (1.43, L1₀). Here, owing to the rarity of Hf and Ta, the CoHf and CoTa alloys were excluded from the candidate list. In addition, we excluded NiCu and CrRh from the list because the large reduction potential difference between the elements in the binary system leads to the unfavorable formation of alloyed structures in which the two elements are homogeneously mixed via a wet-chemical method for nanoparticle (NP) synthesis¹⁷.

Experimental verification of the DFT-guided bimetallic catalysts

For the remaining 13 candidates, we tried to synthesize their alloyed NPs and confirm whether their crystal structures were identical to those (Fig. 3) predicted by DFT calculations. For NP synthesis, we used a butyllithium reduction method¹⁸. Details of the NP synthesis are found in the Methods section. Because it was assumed in Fig. 3 that the proposed alloys had a composition of 50:50, we intended to synthesize alloys with nearly the same composition. Inductively coupled plasma (ICP) analyses revealed that the compositions of the synthesized alloys (loading ratio of metal precursors = 50:50) were $\text{Au}_{51}\text{Pd}_{49}$, $\text{Ni}_{61}\text{Pt}_{39}$, $\text{Pd}_{50}\text{Cu}_{50}$, $\text{Pd}_{52}\text{Ni}_{48}$, $\text{Pt}_{58}\text{Co}_{42}$, $\text{Pt}_{52}\text{Pd}_{48}$, $\text{Rh}_{56}\text{Ni}_{44}$, and $\text{Rh}_{56}\text{Pt}_{44}$; however, CoFe, NiIr, NiMo, NiNb, and NiCo were not alloyed because the reducing power of butyllithium used as a reducing agent was likely insufficient. To confirm whether the alloyed NPs had the same crystal structures as predicted by DFT, their X-ray powder diffraction (XRD) patterns were investigated, as shown in Fig. 4. The samples showed alloyed diffraction patterns without signals from phases of the pure elements that compose each alloy. We also simulated XRD patterns of the alloys on the basis of the DFT crystal structures and found that the simulated patterns matched well with the experimental patterns. This result clearly reveals that we successfully synthesized alloyed NPs with the crystal structures predicted by DFT calculations for eight bimetallic systems. The

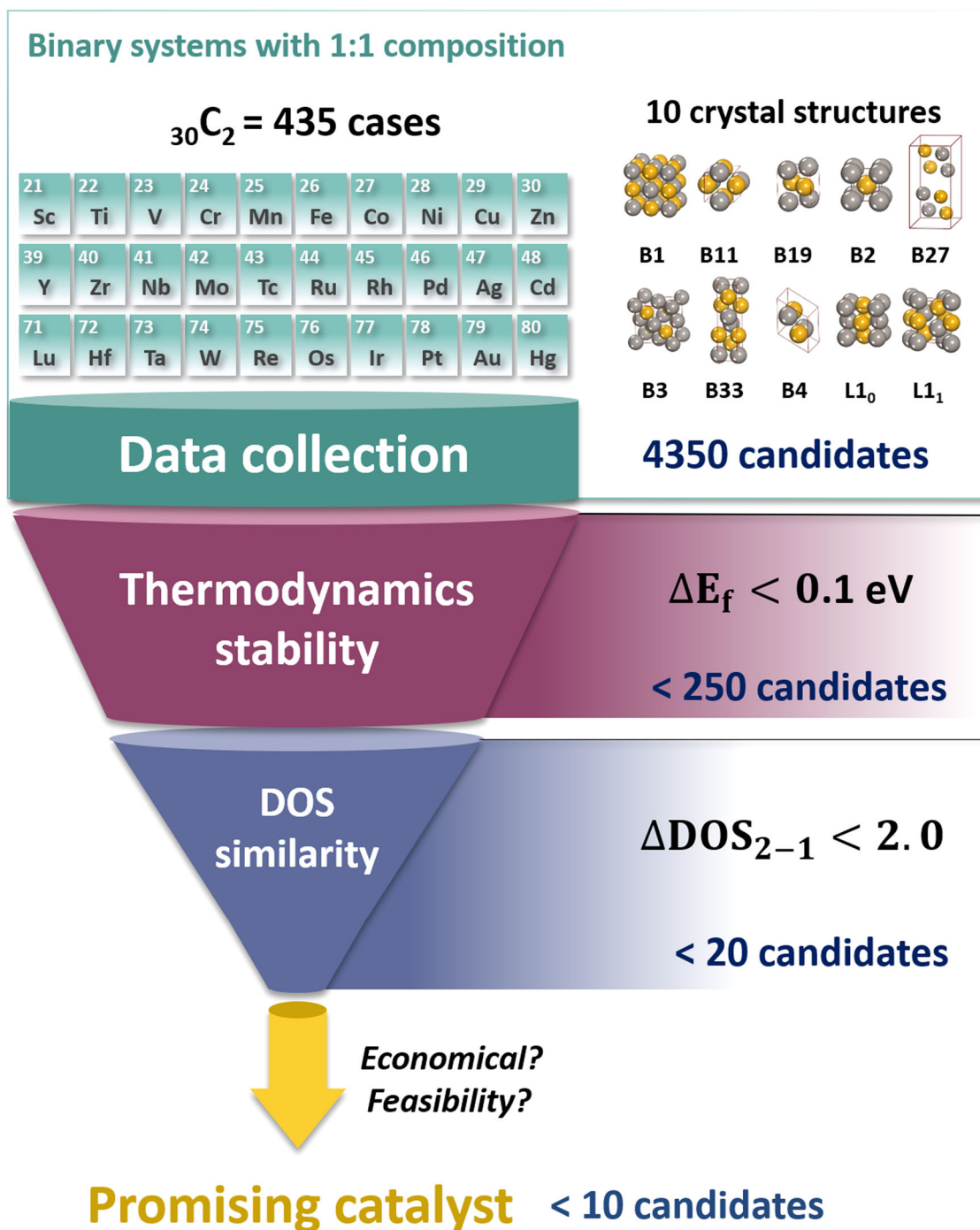


Fig. 1 High-throughput screening protocol for the discovery of bimetallic catalysts. There are three screening steps to identify catalyst candidates from 4350 candidates. The top (cyan color) section indicates the first step showing 30 elements and 10 crystal structures to collect binary alloys with a 1:1 composition. The middle (magenta color) and bottom (violet color) sections indicate the second and the last steps relevant to the thermodynamic stability and the DOS similarity, respectively.

lattice parameters for the alloyed samples are presented in Supplementary Table 1. In addition, we performed Rietveld refinements of the XRD patterns (Supplementary Figure 1). The synthesized NPs clearly have cubic-based structures as predicted by our DFT calculations, although in the Ni-Pt samples a small amount of non-alloyed Pt (pure Pt) coexists with alloyed Ni₇₂Pt₂₈. As we used the synthesized Ni-Pt samples themselves when measuring their catalytic performance, we used the ICP composition (Ni₆₁Pt₃₉).

It was also important to determine whether the synthesized NPs have ordered or disordered structures because the two types of structures can show different catalytic properties¹⁹. The main role of our descriptor (ΔDOS_{2-1}) in the high-throughput protocol for catalyst development is to discover potential catalysts and then transfer the information to experimentalists at high speed. For this purpose, a reference structure for comparison with alloys is required because various structures are possible for random solid-solution structures. In this work, ordered structures were used as a reference and were also validated by comparing simulated and

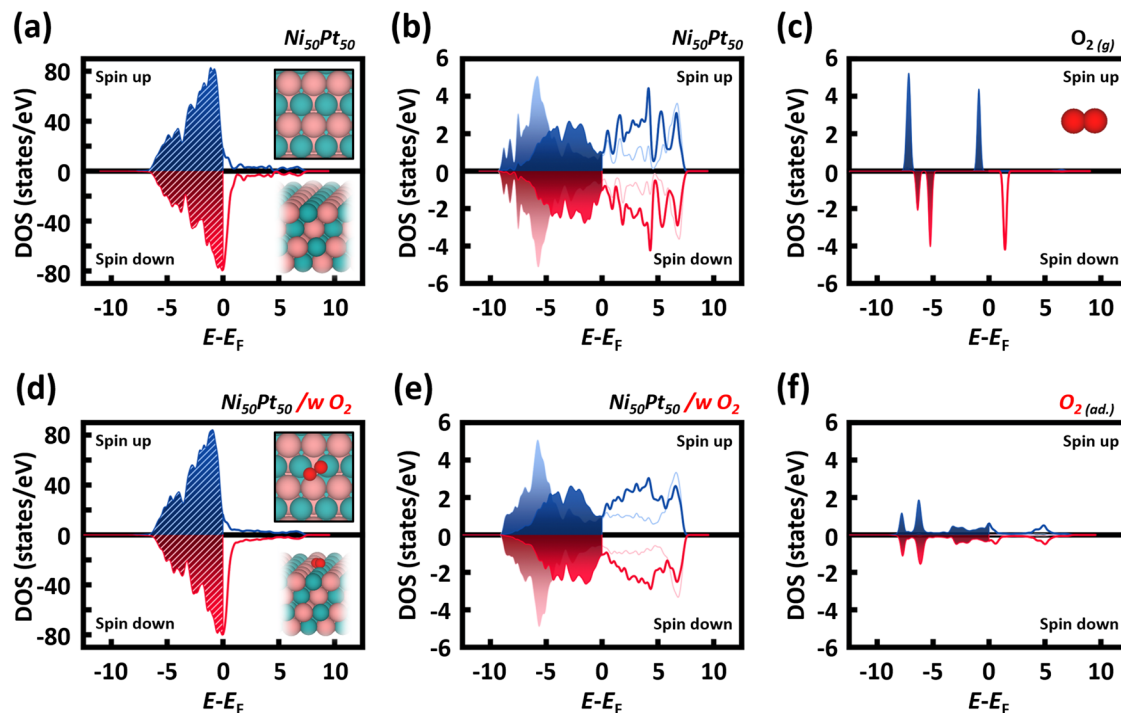


Fig. 2 Partial DOS for the $\text{Ni}_{50}\text{Pt}_{50}$ (111) system before and after O_2 adsorption. The s -states (light), p -states (dark), and d -states (pattered) DOS plots are shown. Occupied states are filled in color; unoccupied states are depicted by lines. **a–c** The shape of states without adsorbed O_2 on the $\text{Ni}_{50}\text{Pt}_{50}$ (111) surface and O_2 gas phase in a vacuum. **d–e** The shape of states of the $\text{Ni}_{50}\text{Pt}_{50}$ (111) surface and O_2 of the adsorbed system.

experimental XRD patterns. From this process, we intended to predict the possibilities and tendencies of alloys for use as H_2O_2 direct synthesis catalysts. Nevertheless, because the synthesized sample could include random solid-solution structures, there is the potential for discrepancies between theory and experiment.

We further characterized the NP samples by high-angle annular dark-field scanning transmission electron microscopy (Fig. 4 and Supplementary Figure 2–9). The elemental color mapping and overlay clearly indicate the homogeneous mixing of elements in each NP. The mean diameters of the alloyed NPs were 3.4 ± 0.4 nm ($\text{Pd}_{50}\text{Cu}_{50}$), 8.8 ± 2.0 nm ($\text{Ni}_{61}\text{Pt}_{39}$), 5.0 ± 1.5 nm ($\text{Rh}_{56}\text{Ni}_{44}$), 11.6 ± 2.0 nm ($\text{Au}_{51}\text{Pd}_{49}$), 5.2 ± 1.5 nm ($\text{Pd}_{52}\text{Ni}_{48}$), 8.1 ± 2.2 nm ($\text{Pt}_{52}\text{Pd}_{48}$), 5.8 ± 1.0 nm ($\text{Pt}_{58}\text{Co}_{42}$), and 1.7 ± 0.2 nm ($\text{Rh}_{56}\text{Pt}_{44}$). In particular, for the four alloys ($\text{Ni}_{61}\text{Pt}_{39}$, $\text{Au}_{51}\text{Pd}_{49}$, $\text{Pd}_{52}\text{Ni}_{48}$, and $\text{Pt}_{52}\text{Pd}_{48}$) showing catalytic properties comparable to those of Pd (Table 1), their NP diameters were in the range of 5.2–11.6 nm, which is similar to the diameter (7.2 ± 1.6 nm) of Pd NPs (Supplementary Figure 10).

To investigate whether the catalytic performance of the eight proposed alloys is comparable to that of Pd, the alloyed catalysts were tested for direct H_2O_2 synthesis under mild conditions (20°C , 1 atm) in comparison to pure Pd (Table 1). Along with the industrial importance of H_2O_2 as an eco-friendly oxidizing agent^{20,21}, the H_2O_2 direct synthesis reaction can be performed under ambient temperature and pressure conditions, and Pd has been regarded as the archetypical catalyst for the chemical reaction although there is still room for performance enhancement²². In terms of H_2O_2 productivity representing the catalytic activity for H_2O_2 direct synthesis, three alloy systems, $\text{Au}_{51}\text{Pd}_{49}$ ($505.2 \text{ mmol}_{\text{H}_2\text{O}_2} \text{ g}_{\text{metal}}^{-1} \text{ h}^{-1}$), $\text{Ni}_{61}\text{Pt}_{39}$ (880.1), and $\text{Pt}_{52}\text{Pd}_{48}$ (1225.6) exhibited performance comparable to that of Pd (552.4). In addition, $\text{Pd}_{52}\text{Ni}_{48}$ showed noticeable H_2O_2 productivity (218.1), although this productivity is lower than that of Pd. Here, it is notable that the four alloy systems have lower ΔDOS_{2-1} values than the alloy systems showing poor catalytic activities. Although the Rh-Ni system has a low ΔDOS_{2-1} value, the DOS patterns near

E_F are quite different from those of Pd (Supplementary Figure 11), which can explain why it shows poor catalytic activity.

On the other hand, the orders of the ΔDOS_{2-1} values and H_2 conversion do not show perfect consistency. However, it is not enough to represent the catalytic performance for H_2O_2 direct synthesis only with H_2 conversion. The H_2O_2 synthesis reaction involves several elementary steps on the catalyst, such as H_2 dissociation and the first and second hydrogenation of O_2 generating OOH and H_2O_2 , respectively. Moreover, when assessing the catalytic performance, side reactions such as H_2O formation should be considered. In other words, the catalytic performance of H_2O_2 direct synthesis is not dominated by only one catalytic behavior but coupled with multiple behaviors that involve not only H_2 conversion but also H_2O_2 productivity and selectivity. In addition, we compared our descriptor of DOS similarity (ΔDOS_{2-1}) with the d -band center that has been widely used in metallic catalysts. Here, we considered the difference between the d -band centers of the alloys and that of Pd ($|\epsilon_{d,\text{Pd}} - \epsilon_{d,i}|$); the d -band centers of the bimetallic alloys are shown in Supplementary Table 4. For comparison, $\text{Pt}_{52}\text{Pd}_{48}$ and $\text{Pd}_{50}\text{Cu}_{50}$ were chosen because they show relatively high and low H_2 conversions, respectively (Table 1). The ΔDOS_{2-1} values appropriately represent the order of H_2 conversion ($\text{Pt}_{52}\text{Pd}_{48}$: $\Delta\text{DOS}_{2-1} = 1.16$ and $\text{Pd}_{50}\text{Cu}_{50}$: $\Delta\text{DOS}_{2-1} = 1.51$), in contrast to the difference in d -band centers ($\text{Pt}_{52}\text{Pd}_{48}$: 0.31 and $\text{Pd}_{50}\text{Cu}_{50}$: 0.08). In this regard, the similarity in DOS patterns can be a good descriptor for the discovery of bimetallic catalysts and needs no calculations relevant to the reaction pathways on the catalyst surfaces, which would require a high computational cost.

Among the four alloy combinations showing high H_2O_2 productivity, the Au-Pd^{13,14,23–25}, Ni-Pd²⁶, and Pd-Pt²⁷ systems were previously reported as promising candidates for H_2O_2 direct synthesis, validating our approach once again. In addition, our approach led to the discovery of a catalyst, a Ni-Pt alloy, which has not yet been reported for H_2O_2 direct synthesis, although the system is well known as an oxygen reduction reaction (ORR) catalyst in fuel cells^{28–30}. As the price of Pd rapidly increases³¹, our

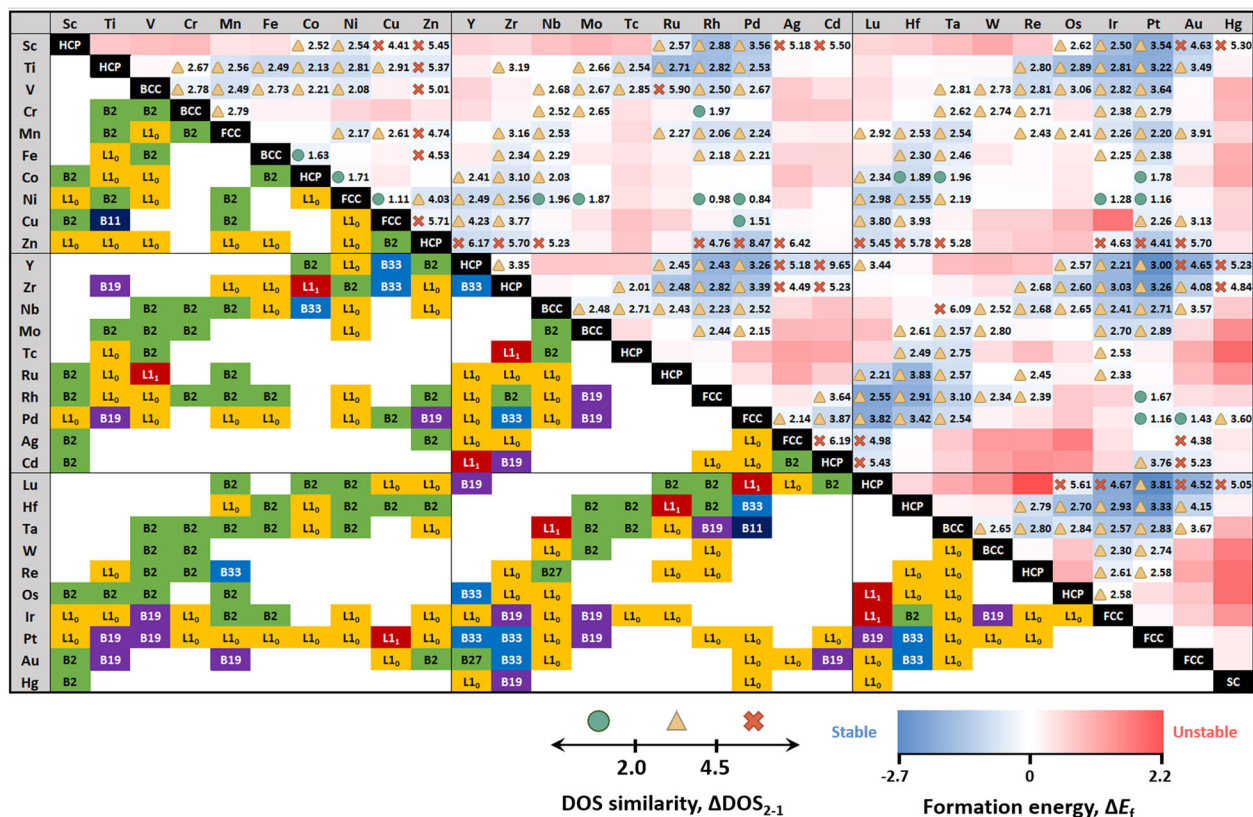


Fig. 3 Map of the thermodynamic stabilities and DOS similarities of bimetallic alloy systems. The diagonal components denote the most thermodynamically stable crystal structures (e.g., FCC, BCC, HCP, and SC) of pure metals. The occupied components under the diagonal denote the most thermodynamically stable crystal structures (e.g., B2, B11, B19, B27, B33, L1₀, and L1₁) of bimetallic alloys. The background colors above the diagonal describe the formation energies, and the occupied components above the diagonal denote the DOS similarity of each alloy compared with Pd(111).

Pd-free Ni-Pt alloy can serve as a more cost-effective option. To identify the cost-effectiveness of the Ni-Pt catalyst, we list the CNP (unit, $\text{mmol}_{\text{H}_2\text{O}_2} \text{ \$metal}^{-1} \text{ h}^{-1}$)³² of the assessed materials in Table 1, in which the metal price [unit, U.S. dollar (\$) instead of catalyst mass is used. In terms of this metric, Ni₆₁Pt₃₉ shows a CNP of 69.3, which is not only ~9.5 times higher than that of Pd (7.3) but also much higher than those of the other candidates (Au₅₁Pd₄₉: 7.1, Pd₅₂Ni₄₈: 5.5, and Pt₅₂Pd₄₈: 23.0). As another metric for catalytic activity, we also considered the turnover frequency of the catalysts. In terms of this metric, Ni₆₁Pt₃₉ (98.5) shows a performance superior to that of Pd (58.8). Moreover, for efficient H₂O₂ direct synthesis, the H₂ conversion and H₂O₂ selectivity properties of the catalysts should be considered. It is also interesting that Ni₆₁Pt₃₉ shows an H₂O₂ selectivity similar to that of Pd, although Ni₆₁Pt₃₉ shows higher H₂ conversion. These findings clearly demonstrate that the Ni-Pt bimetallic catalyst is very attractive for H₂O₂ direct synthesis.

When screening bimetallic catalysts by electronic structure calculations, only one composition (50:50) for the bimetallic systems was considered because DFT prediction to determine the optimized composition to provide the best catalytic performance would be challenging and time-consuming. Instead, composition optimization proceeded with the help of experiments, likely providing a faster result than a DFT prediction. Therefore, to optimize the composition of the Ni-Pt bimetallic catalysts, we also explored the effects of the Ni/Pt ratio in Ni_xPt_{100-x} NPs on their catalytic properties for H₂O₂ direct synthesis (Supplementary Table 2), and no significant structural changes in the Ni_xPt_{100-x} NPs were observed (Supplementary Figure 12 and 13). We found that the best catalytic performance was exhibited by Ni₆₁Pt₃₉ in terms of H₂O₂ productivity, H₂ conversion, and H₂O₂ selectivity.

Catalytic reaction mechanism

The Ni-Pt bimetallic catalysts were proposed based only on electronic structure calculations without any calculations relevant to the reaction pathways. Thus, to justify the experimental catalytic activity shown in Table 1, we investigated the reaction mechanisms on the catalyst surface using DFT calculations. We considered the close-packed (111) surface of the Ni₅₀Pt₅₀ slab in L1₀, where the alloy composition was considered for simplicity of the calculations although the best catalytic performances were experimentally observed for the Ni₆₁Pt₃₉ composition. The Langmuir-Hinshelwood mechanism³³⁻³⁵ involving adsorption of both H₂ and O₂ over a catalyst surface was first explored. Our DFT calculations revealed that dissociative adsorption of H₂ occurs very favorably over Ni₅₀Pt₅₀(111) surfaces (Supplementary Figure 14), which is similar to Pd(111)^{33,34}. This finding implies that the hydrogenation of O₂ over Pd(111) and Ni₅₀Pt₅₀(111) determines the catalytic activity for H₂O₂ synthesis. In Fig. 5a, the overall H₂O₂ synthesis involving two sequential hydrogenations of O₂ (I→II and II→III) is exothermic by 0.42 eV on Ni₅₀Pt₅₀(111), which is more favorable than the value of 0.07 eV for Pd(111). Moreover, while the rate-determining step on Pd(111) is the first hydrogenation (I→II) to form OOH* (*denotes a surface site) with an energy barrier of 0.78 eV, the rate-determining step on Ni₅₀Pt₅₀(111) is observed at the desorption step of the generated H₂O₂*, with an energy barrier of 0.69 eV (III→V). These results indicate that higher H₂O₂ productivity is possible on Ni₆₁Pt₃₉ NPs than on Pd NPs, as observed in Table 1. On the other hand, Wilson and Flaherty³⁶ proposed another mechanism for H₂O₂ formation on Pd NPs called a heterolytic reaction mechanism, similar to the two-electron ORR, in which an electron is generated during the

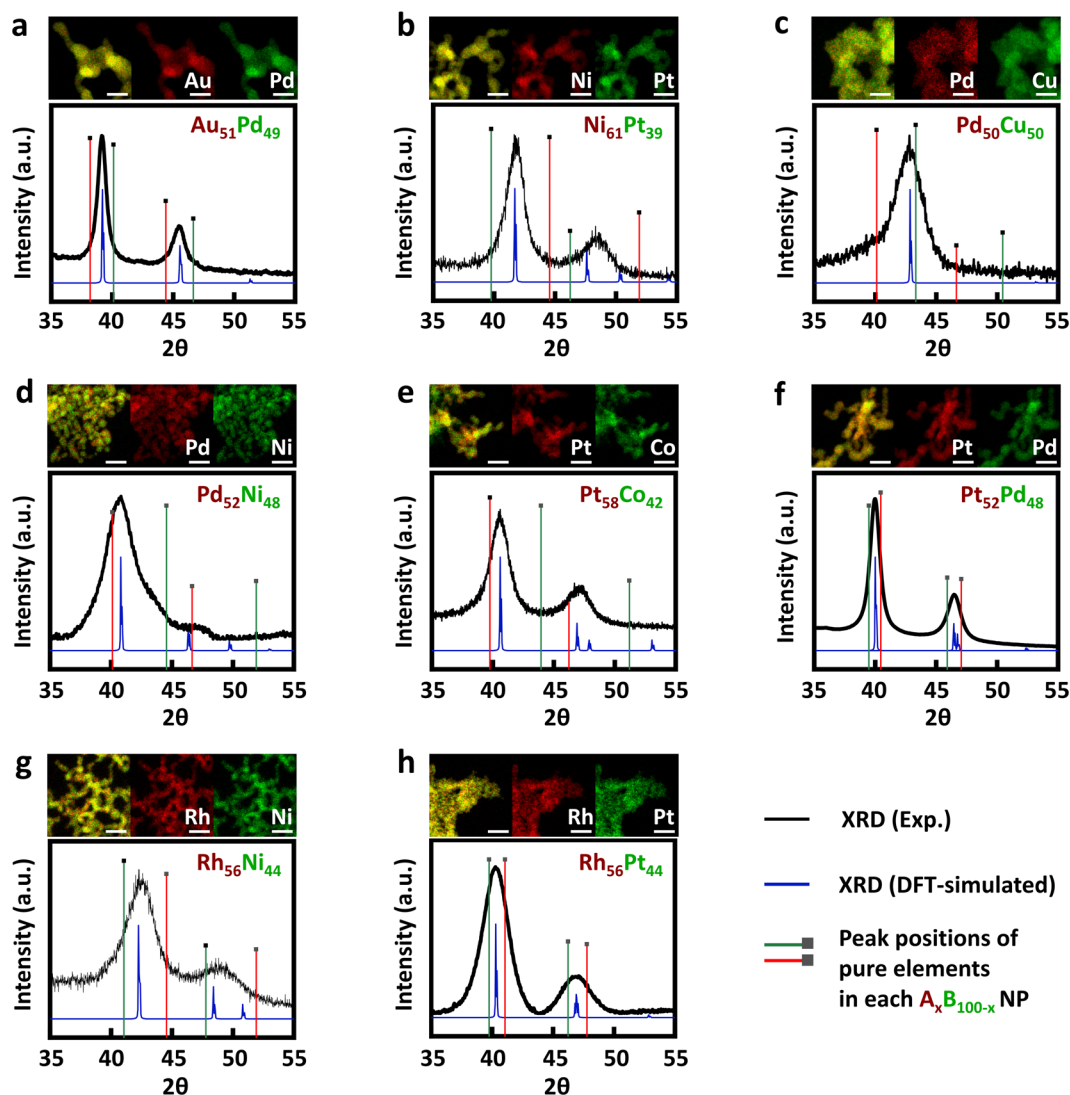


Fig. 4 Characterizations of the synthesized bimetallic NPs. XRDs for **a** Au₅₁Pd₄₉, **b** Ni₆₁Pt₃₉, **c** Pd₅₀Cu₅₀, **d** Pd₅₂Ni₄₈, **e** Pt₅₈Co₄₂, **f** Pt₅₂Pd₄₈, **g** Rh₅₆Ni₄₄, **h** Rh₅₆Pt₄₄ NP samples. For comparison, the red and green lines in the XRD patterns correspond to the peaks of pure elements in each bimetallic NP. The blue peaks were simulated with the crystal structures of the bimetallic system predicted by DFT calculations. Above each XRD pattern, the element mapping images acquired by STEM-EDX are included, where the first image (the most left) is the overlay image of the maps for elements in each bimetallic NP. The scale bars correspond to 20 nm. The enlarged images of the STEM-EDX are also provided in Supplementary Figures 2–9.

oxidation process of H₂ on the NP surfaces. We also investigated the mechanism on Ni₅₀Pt₅₀(111) and Pd(111) by DFT calculations where the computational hydrogen electrode method was used along with consideration of implicit water solvents (Fig. 5b). On both Pd(111) and Ni₅₀Pt₅₀(111), the ORR processes for H₂O₂ formation are thermodynamically favorable. In particular, although the first protonation is very similar (−1.03 eV for Pd and −1.00 eV for Ni₅₀Pt₅₀), the second protonation is slightly more favorable on Ni₅₀Pt₅₀(111) (−1.40 eV vs −1.58 eV). This mechanism also readily reveals more preferential H₂O₂ production on Ni-Pt surfaces than on Pd surfaces.

In Fig. 5a, it is interesting that Ni₅₀Pt₅₀(111) stabilizes H₂O₂* (III state) more than Pd(111) does, whereas the energetics for OOH* (II state) are comparable on the two surfaces. To clarify this result, we investigated the binding characteristics between the adsorbates (OOH* and H₂O₂*) and catalyst surfaces (e.g., Pd(111) and Ni₅₀Pt₅₀(111)) via projected crystal orbital Hamilton population (pCOHP) analysis (Supplementary Figure 15a), in which we display the pCOHPs according to the typical method, namely drawing negative (i.e., bonding) contributions to the right and positive (i.e.,

anti-bonding) contributions to the left. For OOH* binding to Pd(111) and Ni₅₀Pt₅₀(111), the bonding contributions are comparable. In other words, there are three energy windows for the bonding contributions: −3 to −4 eV (1st window), −5 to −7 eV (2nd), and −8 to −9 eV (3rd). Here, the bonding energy levels for the first and third contributions are lower (stronger binding) for Ni₅₀Pt₅₀(111), whereas the bonding energy levels for the second are lower for Pd(111). On the other hand, in the case of H₂O₂* binding, all of the bonding contributions for Ni₅₀Pt₅₀(111) are lower than those for Pd(111), which explains why the H₂O₂* adsorbate is more stable on Ni₅₀Pt₅₀(111) than Pd(111). This behavior can be explained by the back-bonding character between H₂O₂* and Ni₅₀Pt₅₀(111). Alloying of Pt and Ni creates electron-rich Ni atoms in the alloy structure, which leads to back-bonding with the adsorbate (the Ni atom donates electrons to an empty orbital in the adsorbate). This effect is significantly enhanced for H₂O₂* compared to OOH* as the O atom in the adsorbate bonded to metal surfaces is more electron-deficient for H₂O₂* than OOH* due to the additional O-H bond in H₂O₂*. From the charge density difference plot shown in Supplementary Figure

Table 1. Catalytic performances of eight bimetallic NPs proposed by the DFT screening process in comparison with that of pure Pd NPs.

Catalyst	H ₂ O ₂ productivity			H ₂ conversion (%)	H ₂ O ₂ selectivity (%)
	Mass-normalized (mmol/g _{metal} ·h)	Cost-normalized (mmol/\$ _{metal} ·h)	TOF (h ⁻¹)		
Au ₅₁ Pd ₄₉ (1.43) ^a	505.2	7.1	77.1	11.6	70.1
Ni ₆₁ Pt ₃₉ (1.16)	880.1	69.3	98.5	22.9	61.2
Pd ₅₀ Cu ₅₀ (1.51)	49.4	1.3	4.2	1.6	50.8
Pd ₅₂ Ni ₄₈ (0.84)	218.1	5.5	18.2	2.8	>99.9 ^b
Pt ₅₈ Co ₄₂ (1.78)	87.6	4.6	12.1	11.0	12.8
Pt ₅₂ Pd ₄₈ (1.16)	1225.6	23.0	186.9	25.0	78.7
Rh ₅₆ Ni ₄₄ (0.98)	16.8	0.1	1.4	-	-
Rh ₅₆ Pt ₄₄ (1.67)	109.3	0.6	15.7	10.6	16.6
Pd	552.4	7.3	58.8	14.0	63.0

^aThe number in parentheses corresponds to ΔDOS_{-1} for the alloy with a composition of 50:50 shown in Fig. 4.

^bThe high selectivity is mainly caused by the low H₂ conversion property.

15b, we find that Ni atoms on Ni₅₀Pt₅₀ and O atoms in H₂O₂* donate electrons (cyan isosurface) while the O atoms in H₂O₂* also accept electrons (yellow), indicating the back-bonding mode between the metal and H₂O₂.

In addition, we discuss the selectivity of H₂O₂ production on Pd (111) and Ni₅₀Pt₅₀(111) with DFT calculations. It is well known that H₂O production, the side reaction for H₂O₂ production, occurs by the O-O bond dissociation^{27,32–34}. Therefore, we investigated the possible O-O bond scission reactions on the Pd(111) and Ni₅₀Pt₅₀(111) surfaces by DFT calculations, where we considered the ratio of the O-O bond dissociation barrier at several steps to the corresponding hydrogenation step barrier or desorption barrier (O₂* dissociation vs O₂* hydrogenation, OOH* dissociation vs OOH* hydrogenation, and H₂O₂ dissociation vs H₂O₂* desorption) for H₂O₂ production as an estimation for the H₂O₂ selectivity (Supplementary Table 5). We assume that the H₂O production reaction occurs most frequently at the O-O bond scission step with the lowest reaction barrier among the three possible O-O bond scission reactions. Comparing the ratios for the three O-O bond scission reactions, Pd(111) shows the lowest ratio of 0.14 (unitless) at the H₂O₂* scission step, which is similar to that of Ni₅₀Pt₅₀(111) (0.12 at the OOH* scission step). This is consistent with the experimental finding that the selectivity for H₂O₂ production is similar for both Pd (63.0%) and Ni₅₀Pt₅₀ (61.2%).

DISCUSSION

This work demonstrates an efficient computational-experimental screening protocol for the development of bimetallic catalysts to replace conventional Pd catalysts for H₂O₂ direct synthesis. Using this protocol, a Pd-free bimetallic catalyst, Ni₆₁Pt₃₉, was successfully developed. Here, we note that Ni and Pt have not usually been considered in the catalysis field for H₂O₂ direct synthesis because they prefer to dissociate O₂ molecules, which prevents H₂O₂ formation, although Ni-Pd²⁵, Pt-Pd²⁶, and Pt-Ag³⁷ bimetallic catalysts have been reported. The success story of our protocol primarily results from the validity of our descriptor, the similarity of electronic DOS patterns, for catalyst screening. Moreover, one can readily extend our screening protocol by updating a reference material. For example, since the Ni-Pt system shows superior catalytic performance in this work, we can discover other catalysts by using the DOS pattern of the Ni-Pt alloy as a reference, which remains as future work. In this regard, this protocol will immediately provide opportunities for catalyst discovery for the replacement or reduction in the use of the platinum-group metals and then enable the further application of these catalysts to other chemical reactions.

METHODS

Computational details for screening bimetallic catalysts

We generated 10 ordered phases for each bimetallic alloy with a 1:1 composition. Specifically, the crystal structure prototypes were obtained by NaCl (B1), CsCl (B2), zinc blende (B3), wurtzite (B4), TiCu (B11), CdAu (B19), FeB (B27), CrB (B33), AuCu (L1₀), and CuPt (L1₁) compounds from the Material Project³⁸. Here, the initial lattice parameters were replaced by values commensurate with covalent radii of two elements in the target compounds. By means of the DFT optimization process, we collected the most stable bulk phases of 4350 binary alloys. Furthermore, the formation energies (ΔE_f) of all the bulk phases were calculated as follows: $\Delta E_f = E[\text{AB}] - E[\text{A}] - E[\text{B}]$, where $E[\text{AB}]$, $E[\text{A}]$, and $E[\text{B}]$ are the total energies of the bimetallic AB compound, A crystal, and B crystal in the unit cell. For thermodynamically favorable alloys, a close-packed surface of each crystal structure was used for the calculation of the DOS pattern of each alloy. In principle, the close-packed surface of L1₀ is the (111) facet, that of B2 is the (110) facet, and those of other crystal structures are the (001) facet³⁹. The DOS patterns were obtained by the sum of the partial DOSs on the surface atoms.

To investigate thermodynamic stabilities in bulk phases and the DOS patterns of surface atoms, spin-polarized DFT calculations were performed using the Vienna Ab Initio Simulation Package (VASP)⁴⁰ with projector-augmented-wave (PAW) pseudopotentials⁴¹ and the revised Perdew-Burke-Ernzerhof (RPBE) exchange-correlation functional⁴². Then, we used a plane-wave kinetic energy cutoff of 400 eV and Monkhorst-Pack k-point meshes of $8 \times 8 \times 8$ for the bulk systems and $4 \times 4 \times 1$ for the slab systems. The bulk of the $1 \times 1 \times 1$ unit cell and the slab of the 2×2 unit cell with four layers were used. In the slab systems, a vacuum spacing of 15 Å was used to avoid interactions between slabs. All relaxations were performed until the energy change was $>1 \times 10^{-6}$ eV/cell and the forces on the individual atoms were <0.01 eV Å⁻¹.

H₂O₂ formation mechanism

The energy diagrams for H₂O₂ production on the Ni₅₀Pt₅₀(111) surface and Pd(111) surfaces were also calculated by the DFT method. The simulations were performed using the VASP⁴⁰ using the PAW⁴¹ pseudopotentials to describe the potential from the ionic core. For the exchange and correlation terms, we employed the RPBE functional⁴² with Grimme's D3 dispersion correction⁴³. An energy cutoff of 400 eV and Monkhorst-Pack k-point meshes of $3 \times 3 \times 1$ for the slab calculations were used. A large vacuum spacing of 15 Å was used to prevent interslab interactions. The top two layers and the reactant molecules were optimized until the energy change was $<1 \times 10^{-4}$ eV/cell and the force on each atom was less than 0.02 eV Å⁻¹. In the case of the Langmuir-Hinshelwood mechanism, the climbing image nudged elastic band⁴⁴ method was employed to investigate the transition states for the main reaction. For the electron-proton transfer mechanism, the computational hydrogen electrode method⁴⁵ with $U = 0$ V in addition to the water solvation energy calculated with the implicit solvent model implemented within the VASP_{sol} package⁴⁶ was used to construct the energy diagram

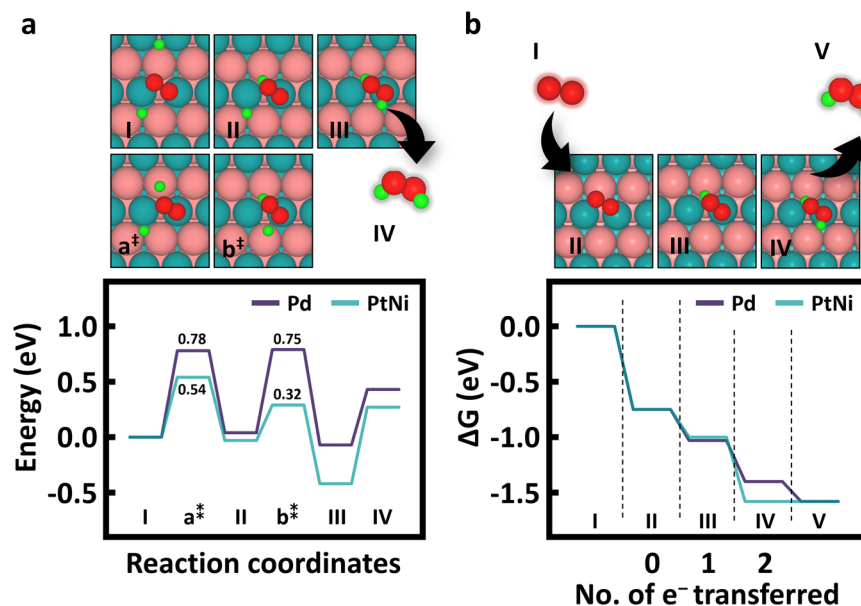
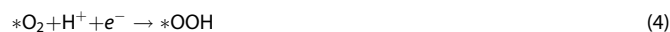


Fig. 5 H_2O_2 direct synthesis mechanisms of $\text{Ni}_{50}\text{Pt}_{50}(111)$ and $\text{Pd}(111)$ from DFT calculations. **a** The Langmuir-Hinshelwood mechanism. **b** The electron-proton transfer mechanism. The cyan lines are the energy diagram for $\text{Ni}_{50}\text{Pt}_{50}(111)$, and the magenta lines are for $\text{Pd}(111)$. The color code for the atoms is as follows: teal = Ni, coral = Pt, red = O, and green = H.

on the following reactions:



We also performed pCOHP calculations⁴⁷ using the LOBSTER package⁴⁸ to understand the binding character between the adsorbates (e.g., OOH^* and H_2O_2^*) and catalyst surfaces (e.g., $\text{Pd}(111)$ and $\text{Ni}_{50}\text{Pt}_{50}(111)$). The differential charge density ($\Delta\rho$) of the H_2O_2^* adsorbates on the $\text{Ni}_{50}\text{Pt}_{50}(111)$ surface was evaluated by the following:

$$\Delta\rho = \rho_{\text{tot}} - \rho_{\text{ads}} - \rho_{\text{slab}} \quad (7)$$

where, ρ_{tot} is the charge density of the H_2O_2^* - $\text{Ni}_{50}\text{Pt}_{50}$ system and ρ_{ads} and ρ_{slab} are the charge densities of the H_2O_2^* adsorbate and metal slab, respectively. The atomic coordinates for ρ_{ads} and ρ_{slab} are equal to those in the H_2O_2^* - $\text{Ni}_{50}\text{Pt}_{50}$ system.

Chemicals

Palladium(II) acetate [$\text{Pd}(\text{CH}_3\text{COO})_2$, $\geq 99.9\%$], copper(II) acetate [$\text{Cu}(\text{CH}_3\text{COO})_2$, 99.99%], nickel(III) acetylacetonate [$\text{Ni}(\text{acac})_3$, 95%], rhodium(III) nitrate hydrate [$\text{Rh}(\text{NO}_3)_3 \cdot \text{XH}_2\text{O}$, ~36%], gold(III) chloride trihydrate [$\text{HAuCl}_4 \cdot 3\text{H}_2\text{O}$, 99.9%], chloroplatinic acid hydrate [$\text{H}_2\text{PtCl}_6 \cdot \text{XH}_2\text{O}$, ~38%], cobalt acetate tetrahydrate [$\text{Co}(\text{CH}_3\text{COO})_4 \cdot 4\text{H}_2\text{O}$, 99.999%], dioctyl ether, oleylamine, and n-butyllithium solution [2.0 M in cyclohexane] were purchased from Sigma-Aldrich. Ethanol was analytical grade and was used without further purification.

Catalyst synthesis

All alloy metal catalysts and Pd catalysts were synthesized using the butyllithium reduction method. To synthesize the bimetallic XY catalysts, 0.017 mmol of X precursor and Y precursor (details are described in Table 3 of Supporting Information) were dissolved in 10 mL of dioctyl ether with 2 mL of oleylamine at 50°C. The solution was then injected into a butyllithium solution containing 15 mL of dioctyl ether and 1.2 mL of 2.0 M butyllithium in cyclohexane at 50°C. The colloids were stirred (500 rpm) for 20 min and then heated to 120°C for 1.5 h in an Ar atmosphere. The reaction mixture was further heated to 260°C for 1 h. The mixture was cooled to room temperature, and 1.25 mL of trioctylphosphine was

injected to protect the colloids. The resulting NPs were washed with ethanol three times.

Catalyst characterization

Transmission electron microscopy (TEM) images and energy-dispersive X-ray spectra (EDS) were acquired using a transmission electron microscope (FEI Talos F200X) equipped with scanning transmission electron microscopy-energy dispersive X-ray spectroscopy (Bruker Super-X EDS system). The crystal structure was examined by X-ray diffraction (Rigaku Dmax 2500) with Cu K α radiation ($\lambda = 1.5406 \text{ \AA}$). The samples for the TEM images and X-ray diffraction patterns were purified by centrifugation three times to remove the surfactants and/or excess reactants. Then, the NPs were dispersed in ethanol. The resulting solution was dropped on a copper grid coated with an amorphous carbon film for the TEM images and a soda-lime-silica glass for the X-ray diffraction pattern. The actual compositions of each alloy catalyst were measured via ICP atomic emission spectrometry using iCAP6500 Duo (Thermo).

Catalyst performance measurements

The direct synthesis of H_2O_2 was performed in a double-jacket glass reactor under stirring at 1200 rpm. The reaction medium (150 ml) was composed of ethanol and water (ethanol:water volume ratio = 1:4) with 0.9 mM sodium bromide (NaBr) and 0.02 M phosphoric acid (H_3PO_4). The catalyst weight used was 1 mg. The volumetric flow rate of the reactant gas stream was 22 ml/min ($\text{H}_2:\text{O}_2$ volume ratio = 1:10). The reaction was performed at 293 K and 1 atm for 1 h. After the reaction, the concentration of H_2O_2 was calculated using iodometric titration. The concentration of H_2 was calculated using gas chromatography (Younglin, 6500GC) equipped with a Molecular Sieve 5 A (Supelco, 60/80 mesh, 6 ft \times 1/8 in, 2.1 mm) packed column and a thermal conductive detector. The catalytic properties (H_2O_2 productivity, H_2 conversion, and H_2O_2 selectivity) shown in Table 1 were calculated with the following equations:

$$\text{H}_2 \text{ conversion}(\%) = \frac{\text{moles of reacted H}_2}{\text{moles of supplied H}_2} \times 100$$

$$\text{H}_2\text{O}_2 \text{ selectivity}(\%) = \frac{\text{moles of formed H}_2\text{O}_2}{\text{moles of reacted H}_2} \times 100$$

$$\text{H}_2\text{O}_2 \text{ productivity}(\text{mmol/g}_{\text{metal}}\text{nh}) = \frac{\text{mmoles of formed H}_2\text{O}_2}{\text{weight of metal}(\text{g}) \times \text{reaction time}(\text{h})}$$

$$\text{TOF}(\text{h}^{-1}) = \frac{\text{mmoles of formed H}_2\text{O}_2}{\text{mmols of metal} \times \text{reaction time}(\text{h})}$$

DATA AVAILABILITY

All data needed to evaluate the conclusions of this paper are available within the paper and Supplementary Information.

Received: 1 April 2021; Accepted: 7 August 2021;

Published online: 20 August 2021

REFERENCES

- Greeley, J. & Mavrikakis, M. Alloy catalysts designed from first principles. *Nat. Mat.* **3**, 810–815 (2004).
- Greeley, J., Jaramillo, T. F., Bonde, J., Chorkendorff, I. & Nørskov, J. K. Computational high-throughput screening of electrocatalytic materials for hydrogen evolution. *Nat. Mat.* **5**, 909–913 (2006).
- Nørskov, J. K., Bligaard, T., Rossmeisl, J. & Christensen, C. H. Towards the computational design of solid catalysts. *Nat. Chem.* **1**, 37–46 (2009).
- Nørskov, J. K., Abild-Pedersen, F., Studt, F. & Bligaard, T. Density functional theory in surface chemistry and catalysis. *Proc. Natl Acad. Sci. USA* **108**, 937–943 (2011).
- Zhao, Z.-J. et al. Theory-guided design of catalytic materials using scaling relationships and reactivity descriptors. *Nat. Rev. Mat.* **4**, 792–804 (2019).
- Xin, H. et al. Effects of d-band shape on the surface reactivity of transition metal alloys. *Phys. Rev. B* **89**, 115114 (2014).
- Ma, X., Li, Z., Achenie, L. E. K. & Xin, H. Machine learning-augmented chemisorption model for CO₂ electroreduction catalyst screening. *J. Phys. Chem. Lett.* **6**, 3528–3533 (2015).
- Xin, H., Holewinski, A. & Linic, S. Predictive structure-reactivity models for rapid screening of Pt-based multimetallic electrocatalysts for the oxygen reduction reaction. *ACS Catal.* **12**, 1–16 (2012).
- Seo, D.-H., Shin, H., Kang, K., Kim, H. & Han, S. S. First-principles design of hydrogen dissociation catalysts based on isoelectronic metal solid solutions. *J. Phys. Chem. Lett.* **5**, 1819–1824 (2014).
- Yang, A. et al. The valence band structure of Ag_xRh_{1-x} alloy nanoparticles. *Appl. Phys. Lett.* **105**, 153109 (2014).
- Kusada, K., Yamauchi, M., Kobayashi, H., Kitagawa, H. & Kubota, Y. Hydrogen-storage properties of solid-solution alloys of immiscible neighboring elements with Pd. *J. Am. Chem. Soc.* **132**, 15896–15898 (2010).
- Pfleiderer, G. & Reidl, H.-J. *Production of hydrogen peroxide*. U.S. Patent 2,158,525 (1939).
- Edwards, J. K. & Hutchings, G. J. Palladium and gold-palladium catalysts for the direct synthesis of hydrogen peroxide. *Angew. Chem. Int. Ed.* **47**, 9192–9198 (2008).
- Edwards, J. K. et al. Switching off hydrogen peroxide hydrogenation in the direct synthesis process. *Science* **323**, 1037–1041 (2009).
- Kobayashi, H. et al. Nanosize-induced drastic drop in equilibrium hydrogen pressure for hydride formation and structural stabilization in Pd-Rh solid-solution alloys. *J. Am. Chem. Soc.* **134**, 12390–12393 (2012).
- Huang, B. et al. Solid-solution alloying of immiscible Ru and Cu with enhanced CO oxidation activity. *J. Am. Chem. Soc.* **139**, 4643–4646 (2017).
- Gilroy, K. D., Ruditskiy, A., Peng, H.-C., Qin, D. & Xia, Y. Bimetallic nanocrystals: synthesis, properties, and applications. *Chem. Rev.* **116**, 10414–10472 (2016).
- Zhou, S. et al. Low-temperature solution-phase synthesis of NiAu alloy nanoparticles via butyllithium reduction: influences of synthesis details and application as the precursor to active Au-NiO/SiO₂ catalysts through proper pretreatment. *J. Phys. Chem. C* **113**, 5758–5765 (2009).
- Ma, S. et al. Electroreduction of carbon dioxide to hydrocarbons using bimetallic Cu-Pd catalysts with different mixing patterns. *J. Am. Chem. Soc.* **139**, 47–50 (2017).
- Campos-Martin, J. M., Blanco-Brieva, G. & Fierro, J. L. G. Hydrogen peroxide synthesis: an outlook beyond the anthraquinone process. *Angew. Chem. Int. Ed.* **45**, 6962–6984 (2006).
- Samanta, C. Direct synthesis of hydrogen peroxide from hydrogen and oxygen: an overview of recent developments in the process. *Appl. Catal. A* **350**, 133–149 (2008).
- Henkel, H. & Weber, W. *Manufacture of hydrogen peroxide*. U.S. Patent 1,108,752, (1914).
- Solsona, B. E. et al. Direct synthesis of hydrogen peroxide from H₂ and O₂ using Al₂O₃ supported Au-Pd catalysts. *Chem. Mater.* **18**, 2689–2695 (2006).
- Edwards, J. K. et al. The effect of heat treatment on the performance and structure of carbon-supported Au-Pd catalysts for the direct synthesis of hydrogen peroxide. *J. Catal.* **292**, 227–238 (2012).
- Edwards, J. K. et al. Effect of acid pre-treatment on AuPd/SiO₂ catalysts for the direct synthesis of hydrogen peroxide. *Catal. Sci. Technol.* **3**, 812–818 (2013).
- Maity, S. & Eswaramoorthy, M. Ni-Pd bimetallic catalysts for the direct synthesis of H₂O₂ - unusual enhancement of Pd activity in the presence of Ni. *J. Mater. Chem. A* **4**, 3233–3237 (2016).
- Sterchele, S. et al. Pd-Au and Pd-Pt catalysts for the direct synthesis of hydrogen peroxide in absence of selectivity enhancers. *Appl. Catal. A* **468**, 160–174 (2013).
- Stamenkovic, V. R. et al. Improved oxygen reduction activity on Pt₃Ni(111) via increased surface site availability. *Science* **315**, 493–497 (2007).
- Becknell, N. et al. Atomic structure of Pt₃Ni nanoframe electrocatalysts by in situ x-ray absorption spectroscopy. *J. Am. Chem. Soc.* **137**, 15817–15824 (2015).
- Tian, X. et al. Engineering bunched Pt-Ni alloy nanocages for efficient oxygen reduction in practical fuel cells. *Science* **366**, 850–856 (2019).
- The metal prices are from the InvestmentMine webpage (<http://www.infomine.com/investment/metal-prices/>).
- Kim, D. et al. Unlocking the potential of nanoparticles composed of immiscible elements for direct H₂O₂ synthesis. *ACS Catal.* **9**, 8702–8711 (2019).
- Li, J., Ishihara, T. & Yoshizawa, K. Theoretical revisit of the direct synthesis of H₂O₂ on Pd and Au@Pd surfaces: a comprehensive mechanistic study. *J. Phys. Chem. C* **115**, 25359–25367 (2011).
- Song, X. et al. Facet-dependent of catalytic selectivity: the case of H₂O₂ direct synthesis on Pd surfaces. *J. Phys. Chem. C* **123**, 26324–26337 (2019).
- Wang, F., Xia, C., de Visser, S. P. & Wang, Y. How does the oxidation state of palladium surfaces affect the reactivity and selectivity of direct synthesis of hydrogen peroxide from hydrogen and oxygen gases? a density functional study. *J. Am. Chem. Soc.* **141**, 901–910 (2019).
- Wilson, N. M. & Flaherty, D. W. Mechanism for the direct synthesis of H₂O₂ on Pd clusters: heterolytic reaction pathways at the liquid–solid interface. *J. Am. Chem. Soc.* **138**, 574–586 (2016).
- Wilson, N. M. et al. Direct synthesis of H₂O₂ on AgPt octahedra: the importance of Ag–Pt coordination for high H₂O₂ selectivity. *ACS Catal.* **8**, 2880–2889 (2018).
- Jain, A. et al. The materials project: a materials genome approach to accelerating materials innovation. *APL Mater.* **1**, 1–11 (2013).
- Tran, R. et al. Surface energies of elemental crystals. *Sci. Data* **3**, 160080 (2016).
- Kresse, G. & Furthmüller, J. Efficiency of ab-initio total energy calculations for metals and semiconductors using a plane-wave basis set. *Comput. Mater. Sci.* **6**, 15–50 (1996).
- Kresse, G. & Joubert, D. From ultrasoft pseudopotentials to the projector augmented-wave method. *Phys. Rev. B: Condens. Matter Mater. Phys.* **59**, 1758–1775 (1999).
- Hammer, B., Hansen, L. B. & Nørskov, J. K. Improved adsorption energetics within density-functional theory using revised Perdew-Burke-Ernzerhof functionals. *Phys. Rev. B: Condens. Matter Mater. Phys.* **59**, 7413–7421 (1999).
- Moellmann, J. & Grimme, S. DFT-D3 study of some molecular crystals. *J. Phys. Chem. C* **118**, 7615–7621 (2014).
- Henkelman, G., Uberuaga, B. P. & Jónsson, H. A climbing image nudged elastic band method for finding saddle points and minimum energy paths. *J. Chem. Phys.* **113**, 9901 (2000).
- Nørskov, J. K. et al. Origin of the overpotential for oxygen reduction at a fuel-cell cathode. *J. Phys. Chem. B* **108**, 17886–17892 (2004).
- Mathew, K. & Hennig, R. G. VASPsol - Solvation model for the plane wave DFT code VASP. <https://github.com/henniggroup/VASPsol> (2015).
- Deringer, V. L., Tchougreff, A. L. & Dronskowski, R. Crystal orbital Hamilton population (COHP) analysis as projected from plane-wave basis sets. *J. Phys. Chem. A* **115**, 5461–5466 (2011).
- Maintz, S., Deringer, V. L., Tchougreff, A. L. & Dronskowski, R. LOBSTER: a tool to extract chemical bonding from plane-wave based DFT. *J. Comput. Chem.* **37**, 1030–1035 (2016).

ACKNOWLEDGEMENTS

This work was supported by Creative Materials Discovery Program through the National Research Foundation of Korea (NRF-2016M3D1A1021141). We acknowledge the financial supports of the Korea Institute of Science and Technology (Grant no. 2E30460).

AUTHOR CONTRIBUTIONS

S.S.H. conceived the idea. B.C.Y., Hyunji Nam, S.Y.L., and S.S.H. designed the calculations and experiments. B.C.Y. performed the high-throughput DFT calculations. Hyunji Nam and Hyobin Nam performed the synthesis and characterization of NP catalysts. Hyunji Nam, Hyobin Nam, K.-Y.L., S.-C.K., and S.O.W. performed the catalytic performance measurements. M.-C.K., H.W.L., and D.K. performed DFT calculations on the catalytic reaction mechanism. B.C.Y., Hyunji Nam, M.-C.K., H.W.L., S.Y.L., and S.S.H.

analyzed and discussed the results. B.C.Y., Hyunji Nam, M.-C.K., S.Y.L., and S.S.H. drafted the manuscript. S.Y.L. and S.S.H. supervised the research. All the authors approved the final version of the manuscript. B.C.Y. and Hyunji Nam contributed equally to this work.

COMPETING INTERESTS

The authors declare no competing interests.

ADDITIONAL INFORMATION

Supplementary information The online version contains supplementary material available at <https://doi.org/10.1038/s41524-021-00605-6>.

Correspondence and requests for materials should be addressed to S.Y.L. or S.S.H.

Reprints and permission information is available at <http://www.nature.com/reprints>

Publisher's note Springer Nature remains neutral with regard to jurisdictional claims in published maps and institutional affiliations.



Open Access This article is licensed under a Creative Commons Attribution 4.0 International License, which permits use, sharing, adaptation, distribution and reproduction in any medium or format, as long as you give appropriate credit to the original author(s) and the source, provide a link to the Creative Commons license, and indicate if changes were made. The images or other third party material in this article are included in the article's Creative Commons license, unless indicated otherwise in a credit line to the material. If material is not included in the article's Creative Commons license and your intended use is not permitted by statutory regulation or exceeds the permitted use, you will need to obtain permission directly from the copyright holder. To view a copy of this license, visit <http://creativecommons.org/licenses/by/4.0/>.

© The Author(s) 2021